The Astrophysical Journal, 977:39 (9pp), 2024 December 10 https://doi.org/10.3847/1538-4357/ad7d05

Radial Evolution of Non-Maxwellian Electron Populations Derived from Quasi-thermal Noise Spectroscopy: Parker Solar Probe Observations

Xianming Zheng[1,2], Mihailo M. Martinović[3], Viviane Pierrard[4,5], Kristopher G. Klein[3], Mingzhe Liu[6,7], Joel B. Abraham[8], Yong Liu[1], Jingting Luo[1], Xiaodong Lin[1], Guoqing Liu[1], and Jingchun Li[1]
[1] Shenzhen Key Laboratory of Nuclear and Radiation Safety, Institute for Advanced Study in Nuclear Energy & Safety, College of Physics and Optoelectronic Engineering, Shenzhen University, Shenzhen 518060, People's Republic of China; lijc@szu.edu.cn
[2] Department of Earth and Space Sciences, Southern University of Science and Technology, Shenzhen, People's Republic of China
[3] Lunar and Planetary Laboratory, University of Arizona, Tucson, AZ 85721, USA; mmartinovic@arizona.edu
[4] Royal Belgian Institute for Space Aeronomy (BIRA-IASB), Space Physics, Solar-Terrestrial Center of Excellence, Brussels, Belgium
[5] Center for Space Radiation (CSR), Earth and Life Institute—Climate Sciences (ELI-C), Université Catholique de Louvain, Louvain–la-Neuve, Belgium
[6] LESIA, Observatoire de Paris, Meudon, France
[7] Space Sciences Laboratory, University of California, Berkeley, CA 94720-7450, USA
[8] Mullard Space Science Laboratory University College London, Holmbury St. Mary, Dorking RH5 6NT, UK
Received 2024 July 8; revised 2024 September 16; accepted 2024 September 17; published 2024 November 29

Abstract

Understanding the transport of energy within space plasmas, particularly in the solar wind, remains a complex challenge. Accurate measurement of electron temperatures and their nonthermal characteristics is crucial for comprehending energy transport properties in plasmas. Quasi-thermal-noise (QTN) spectroscopy has emerged as a dependable tool for precise electron parameters assessment as it is less susceptible to spacecraft effects than particle detectors. In this study, we apply a QTN spectroscopy fitting method to analyze data from the Parker Solar Probe FIELDS radio instrument obtained during Encounters 2 through 13, under unbiased antenna conditions. We use the kappa function to characterize the electron velocity distribution and employ a fitting technique to derive the changes in each parameter across heliocentric distances ranging from 12 Rs to 76 Rs. Specifically, we find that the electron density scales as $n_e \propto r^{-2.09\pm0.04}$ and the $T_e \propto r^{-0.65\pm0.02}$. The distribution of the kappa index has three distinct regions as a function of radial distance from the Sun. Furthermore, we conduct a statistical analysis of solar wind energy flux which we finds follows a power-law relationship $w_{\rm total} \propto r^{-1.92\pm0.04}$.

Unified Astronomy Thesaurus concepts: Space probes (1545)

1. Introduction

The solar wind, an intricate and continuous exodus of highly ionized plasma from the solar corona, constitutes of a mixture of protons, α-particles, traces of heavy ions, and electrons. The majority of momentum flux within the solar wind can be attributed to ions, owing to their larger mass, which plays an important role in shaping solar wind dynamics (D. Verscharen et al. 2019). Electrons, being comparatively lighter, assume the primary role as carriers of heat flux due to their higher thermal velocities (E. Marsch 2006; G. Le Chat et al. 2009). Therefore, electrons are expected to play a key role in the thermally driven expansion of the solar wind. Thus, having an accurately measured electron temperature radial profile is of prime interest for quantifying the energy transport in the solar wind and serves as an important ingredient to constrain thermally driven solar wind models (E. N. Parker 1958; V. Pierrard & J. Lemaire 1996; M. Maksimovic et al. 1997a; I. Zouganelis et al. 2004).

To simplify matters, the observation of solar wind electron temperatures can be described by a power law as a function of the distance r from the Sun. This power law dependence varies between isothermal and adiabatic models (M. Maksimovic et al. 2000); describing the electron temperature as $T_e = T_0 r^{\alpha}$, α is observed to range between 0 (isothermal) and $-4/3$ (adiabatic). For the kinetic temperature, α is found between -0.2 and -0.9 (E. Marsch et al. 1989; W. G. Pilipp et al. 1990), whereas for the electron core temperature, α is found between -0.3 and -1.1 (M. Maksimovic et al. 1995; J. L. Phillips et al. 1995; K. Issautier et al. 1998). The considerable variation in the α measurements is to be expected and arises from multiple factors (G. Le Chat et al. 2011; M. Liu et al. 2023).

(i) It is difficult to separate genuine radial variations along stream flux tubes from those across them.
(ii) Transient structures such as coronal mass ejections, co-rotating interaction regions, and interplanetary shocks introduce significant variation.
(iii) The observations have been carried out over different latitudinal and radial ranges during different phases of the solar activity.
(iv) Many different data acquisition, reduction, and fitting techniques that leverage different observable quantities have been used.

Quasi-thermal-noise (QTN) spectroscopy, theoretically described more than half a century ago (J. A. Fejer & J. R. Kan 1969), can yield accurate electron density and temperature measurements using observations of the plasma peak in electric field spectra in the solar wind. It has been used in many space missions, including the ISEE-3, Ulysses, Wind, and STEREO missions (N. Meyer-Vernet 1979; S. Hoang et al. 1980; P. J. Kellogg 1981; K. Issautier et al. 1999, 2005; M. Moncuquet et al. 2005; I. Zouganelis et al. 2010; M. M. Martinović et al. 2016, 2020). Recent investigations (M. Maksimovic et al. 2020; M. Moncuquet et al. 2020; M. M. Martinović et al. 2022; M. Liu et al. 2023) have applied this

technique to Parker Solar Probe (PSP) electric voltage spectra acquired by the Radio Frequency Spectrometer (RFS/FIELDS; S. D. Bale et al. 2016; M. Pulupa et al. 2017). Typical particle analyzers are affected by spacecraft photoelectrons and charging effects. Since the QTN electron density is deduced from a peak in the electric potential-frequency spectrum, this measurement is independent of gain calibration and spacecraft charging. Due to its reliability and accuracy, the electron number density derived from the QTN spectroscopy is called the "gold standard" for total density and is routinely used to calibrate other instruments (M. Maksimovic et al. 1995; C. Salem et al. 2001; K. Issautier et al. 2001; P. L. Whittlesey et al. 2020). The electron number density determined using the QTN technique on PSP has served as a benchmark calibration standard for scientific analyses.

In this paper, we present our methodology for calculating QTN spectroscopy assuming the electron velocity distributions are well described by kappa functions, which is elaborated in Section 2. We employ this method to analyze a subset of the data collected by the PSP/FIELDS instrument, deriving plasma density and total electron temperature, as expounded in Section 3. Our primary aim is to unveil the radial variations observed in the kappa index and solar wind energy flux using PSP measurements from Encounters 2 through 13, covering heliocentric distances ranging from 12 Rs to 76 Rs (where Rs denotes the Solar radius), as discussed in Section 4. In Section 5, we wrap up with a comprehensive discussion encompassing future model prospects and an assessment of potential limitations of the methodology.

2. Methodology

2.1. FIELDS Instrument Observation

We utilized the RFS component of the FIELDS (S. D. Bale et al. 2016) suite onboard PSP to collect electric field fluctuation data within a specified frequency range. The RFS comprises both low-frequency receivers and high-frequency receivers, covering frequency ranges of 10 kHz–1.7 MHz and 1.3–19.2 MHz (M. Pulupa et al. 2017), respectively. Each receiver is equipped with 64 logarithmically spaced frequency bins, providing an approximate resolution of 4.5%, and maintaining the statistical uncertainty of the power in each averaged spectrum below 0.3 dB. During certain segments of each Encounter, a bias current was applied to the antennas to maintain their potential close to that of the undisturbed plasma. As this biasing impacts the electric field spectra, all signals collected during compensation bias intervals are not included in this study. Consequently, our analysis concentrates exclusively on the intervals when the FIELDS antenna remains unbiased. This option remained viable throughout the entire period from PSP E2 to E13 that we are interested in. Unlike previous methods, our fitting range includes the peak frequency interval, allowing for the calculation of solar wind density and the Kappa index.

To streamline the calculations, we began by determining plasma density through peak tracking and computed it as $n_e \sim f_p^2$, as described in D. A. Gurnett (1998) and S. D. Bale et al. (2019). Subsequently, we conducted a fitting process to determine the total electron temperature, utilizing signals ranging from $3f_p$ to above 1.6 MHz, while excluding the resistively coupled antenna mechanism, following the method outlined in the paper (M. Maksimovic et al. 2020). Lastly, we carried out a fitting procedure for the κ index using the spectrum spanning from $0.8f_p$ to $3f_p$. This spectrum was derived from 1 minute median filter to eliminate signal contamination from various high-frequency sources, including Langmuir wave bursts and pollution from unidentified sources. Because these fluctuations are just transient disturbances and fast fluctuations, and due to limited availability of QTN data, we are using manual removal to eliminate the radio emission signal.

2.2. Quasi-thermal Noise Spectroscopy

A passive electric field antenna registers variations in the electric potential generated by the movements of surrounding electrons and ions. The synthetic QTN spectrum, denoted as $V^2(f)$, is computed through the summation of individual contributions from electrons, protons, impact (shot) noise, instrument noise, and galaxy radiation as follows:

$$V^2 = \Gamma^2(V_{\rm qtn}^2 + V_{\rm pn}^2 + V_{\rm sn}^2 + V_{\rm gal}^2) + V_{\rm noise}^2, \quad (1)$$

where $V_{\rm qtn}^2$, $V_{\rm pn}^2$, $V_{\rm sn}^2$, $V_{\rm gal}^2$, $V_{\rm noise}^2$ represent the electron QTN, the Doppler-shifted proton thermal noise, the shot noise, the galactic radio background noise, and instrument noise, respectively. The instrument noise is estimated $V_{\rm noise}^2 \approx 2.3{*}10^{-17}V^2/\mathrm{Hz}$ (S. D. Bale et al. 2016; M. Maksimovic et al. 2020). Γ is the antenna gain of the receiver, which is expressed as $\Gamma^2 = \frac{C_a^2}{(C_a+C_s)^2}$. Here, C_a and C_s are the dipole antenna capacitance and the stray capacitance. For the frequency ranges considered, $C_a = \frac{\pi\epsilon_0 L}{\ln(\frac{L}{a})-1}$ (N. Meyer-Vernet et al. 2017) and $C_B \approx 18$ pF (M. Moncuquet et al. 2020), where $L = 2$ m is the length of antenna, $a = 1.5\times10^{-3}$ m is the wire radius, and ϵ_0 is the vacuum permittivity. For an isotropic Maxwellian, the electron contribution is (N. Meyer-Vernet & C. Perche 1989)

$$V_{\rm qtn}^2(\omega) = \frac{16m_e\omega_p^2}{\pi\epsilon_0}\int_0^\infty \frac{B(k,\omega)F(k)}{k^2\,|\epsilon_L(k,\omega)|^2}dk, \quad (2)$$

$$B(k,\omega) = \frac{2\pi}{k}\int_{\frac{\omega}{k}}^\infty vf(v)dv. \quad (3)$$

Here, $f(v)$ represents the electron Velocity Distribution Function (eVDF) and $\epsilon_L(k,\omega)$ denotes the plasma longitudinal function, where k and ω denote the wavenumber and angular frequency, respectively. More detail are described in the paper (M. Martinović 2016), such as the $B(k)$ and ω_p (the angular frequency of plasma oscillation). The $F(k)$ Antenna Response Function is based on model results (M. M. Martinović et al. 2022), which we will refer to as "M22" in the following section. In the analysis of QTN, eVDFs have often been modeled as a combination of two Maxwellian functions (K. Issautier et al. 2004, 2008). However, this type of velocity distribution does not adequately capture the behavior of superthermal electrons (Y. F. Chateau & N. Meyer-Vernet 1991; V. Pierrard & M. Lazar 2010). Therefore, in this paper, we employ a theoretical approach to calculate QTN, using a kappa function to describe the electron velocity distribution (G. Le Chat et al. 2009, 2010). The isotropic kappa

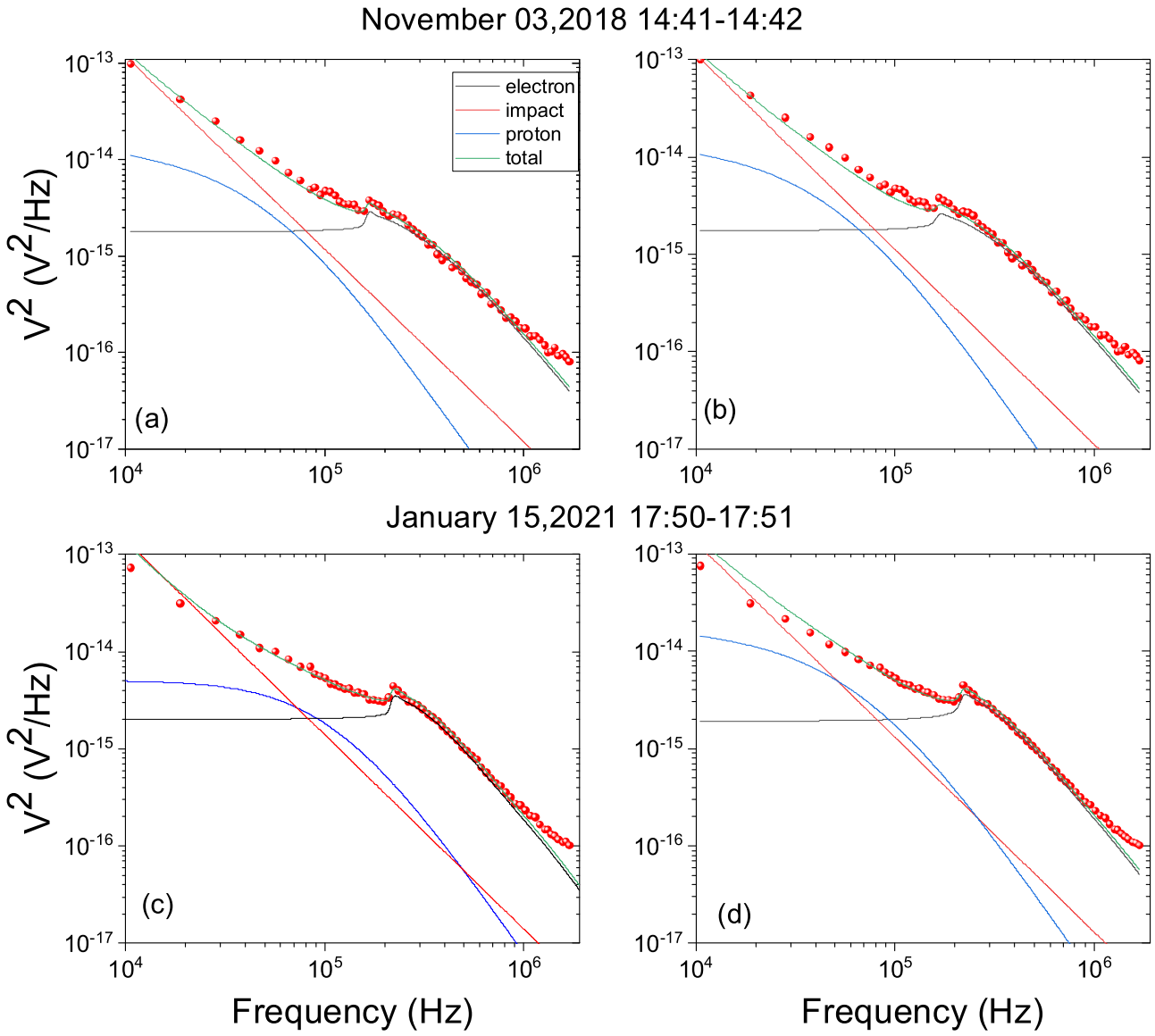

Figure 1. Example QTN fitting results using different eVDF models are shown, with the red dots representing the observations made by PSP. Panel (a) displays the results presented in M. Maksimovic et al. (2020), while (b) showcases our fitted results. The fitting procedure is detailed in Section 2.1. Both sets of results demonstrate a high degree of concurrence. Panels (c) and (d) compare results for a different interval between the two Maxwellian fit and kappa fit.

velocity distribution is defined as follows:

$$f_k(v) = \frac{\Gamma(\kappa+1)}{(\pi\kappa)^{\frac{3}{2}} v_0^3 \Gamma\left(\kappa-\frac{1}{2}\right)}\left(1+\frac{v^2}{\kappa v_0^2}\right)^{-\kappa-1}, \quad (4)$$

where Γ denotes the gamma function, v_0 is the thermal speed related to the kinetic temperature $v_0 = \sqrt{\left(\frac{2\kappa-3}{\kappa}\right)\left(\frac{k_B T_e}{m_e}\right)}$, k_B is the Boltzmann constant, and m_e is the electron mass.

To determine the effective electron QTN spectroscopy, we rely on model results (J. C. Novaco & L. W. Brown 1978; A. Zaslavsky et al. 2011) to calculate the contributions of galaxy radiation power. The background radio galactic noise is modeled as $V^2_{\rm galaxy} = \frac{4\pi}{3} Z_0 \Gamma_R^2 L_{\rm eff}^2 B_{\rm model}$, where $Z_0 = 120\,\pi$ is the impedance of vacuum, $\Gamma_R L_{\rm eff} = 1.17$ is the reduced effective length, and $B_{\rm model}$ is the empirical model for the isotropic sky background brightness, which is $B_{\rm model} = B_0 f_{\rm MHz}^{-0.76} e^{\tau}$. Here $B_0 = 1.38 * \frac{10^{-19}\rm W}{\rm m^2\,Hz\,sr}$, $\tau = 3.28 f_{\rm MHz}^{-0.64}$ are best-fit parameters.

Figure 1 depicts standard power spectral density RFS spanning from 100 kHz to 1.7 MHz, measured by the FIELDS V1–V2 antenna dipole. The red data points signify observations obtained from PSP, which were processed using 1 minute median values; i.e., each point in frequency is being averaged over a minute. In every inversion calculation, it is imperative to initially deduct the influences of galaxy radiation and instrument noise (both of them are constants, which we have not plotted in the Figure 1). This necessitates acquiring a pristine QTN spectrum, ensuring its composition solely comprises electron, proton, and impact noise. As you can see the black line is the electron QTN, the red and blue lines represent impact/shot noise and proton noise, respectively. Panels (c) and (d) display the results of comparing the kappa eVDF with the two-Maxwellian eVDF results. It is important to note that, within this context, we have constrained our kappa index to positive integers less than 15, with lower bound of 1.5 due to the definition of the eVDF.

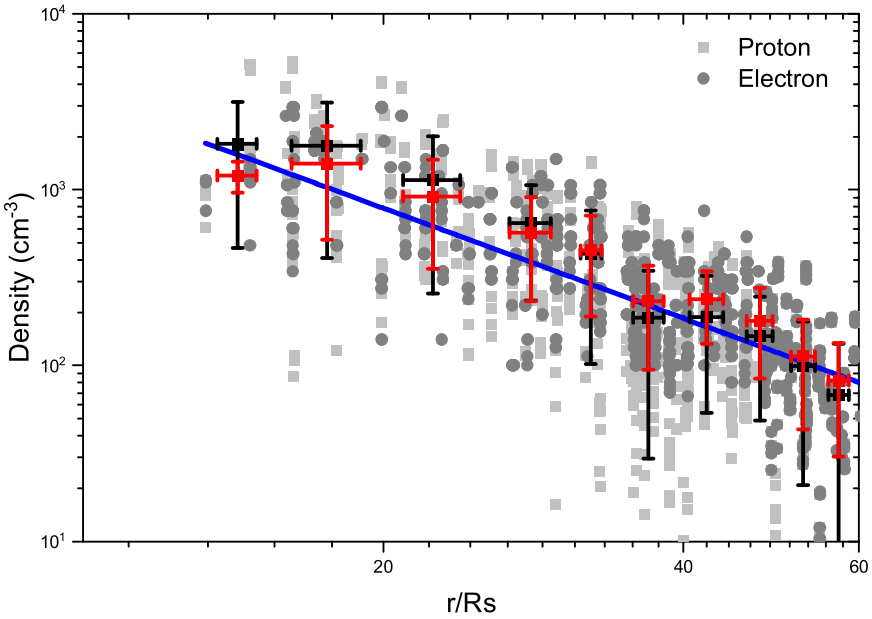

Figure 2. Radial variation of electron density within the selected data range. The gray boxes represent proton density data obtained from SPAN-I measurements (moments), while the dark gray dots represent the fitting results derived through QTN spectroscopy. The electron density (n_e) is fitted using a power-law expression: $n_e = n_0(r)^{-\eta}$ (depicted by the blue line). Notably, both sets of results exhibit a consistent trend. The red and black dots (protons and electrons respectively) show the density averages at a distance of 5 Rs for each bin.

3. Deducing the Electron Density and Temperature

3.1. Electron Density

In this section, we utilize the kappa velocity distribution, Equation (4), along with the M22 antenna response model to derive eVDF parameters from QTN spectra acquired from PSP measurements during encounters 2 through 13. This calculation fits these spectra to the 1 minute median values of RFS data, which were sampled using the unbiased V1–V2 dipole. Given the substantial number of spectra sampled during each of these intervals, it is worth noting that each panel in Figure 1 corresponds to a median of approximately 10 to 15 downloaded spectra. For each of the spectra, we employ the SL algorithm (X. Zheng et al. 2024; combining the steepest descent and Levenberg–Marquardt methods) to fit the spectra at their full resolution.

The data was binned into 14 radial distance intervals of equal width in linear space, each separated by a distance of 5 Rs. In each of these radial bins, we computed the average (mean value) and standard deviation of the relevant parameters. The later we use as our estimate for the uncertainty in each radial bin.

Figure 2 depicts the median values of n_e, which were determined by tracking the plasma line at f_p, and we have removed any questionable measurements (especial the Langmuir wave and radio emission as described in M. Liu 2022). This algorithm draws inspiration from the Spectroscopie Ondes and Bruit Electronstatique Thermique radio receiver (M. Moncuquet et al. 2006) utilized during the BepiColombo mission. The core principle of this algorithm revolves around identifying the change in the amplitude within each raw spectrum. The results show that the electron density varies as $n_e = 6.2 \times 10^5\,(r)^{-2.09}$, which is consistent with our prior work where we calculated $n_e = 5.54 \times 10^5\,(r)^{-2.08}$. The gray squares represent the SPAN-I (R. Livi et al. 2022) measurements of protons compared to the QTN results. The SPAN-I instrument from the SWEAP suite is designed to measure the velocity distribution functions of solar wind protons and alphas. Densities measured by SPAN-I are lower than the QTN results, which may be due to the charge density of other ions, such as alpha particles, in the solar wind, or a limited instrument field of view (L. Woodham et al. 2021).

3.2. Total Electron Temperature

Figure 3 illustrates the total electron temperature, T_e, derived from the QTN spectroscopy using a kappa function with the selected data set, as a function of heliocentric distance. The results from M20 (M. Moncuquet et al. 2020) denoted by red line, show $T_c(\mathrm{eV}) \approx 418r^{-0.74}$, while the results from L23 (M. Liu et al. 2023) denoted by blue line, depict $T_e = (491.7 \pm 61.0)r^{-0.66\pm0.09}$. According to the relationship $T_e \approx T_c(1 + a_h\,t_h;\ \ a_h = n_h/n_c,\ \ t_h = T_h/T_c)$, the expression $a_h\,t_h = 1.17\,r^{0.07}$ is derived from previous results. However, in our fitting results, we assumed $a_h = 0.05$, and $t_h = 2$ (resulting in $a_h\,t_h < 0.17$), following previous results (Š. Štverák et al. 2009). This assumption implies that the M20 result will be smaller than the results of our fitting. This discrepancy is evident in the figure. Consequently, based on the differences in T_c values between our results and M20, it is apparent that we are underestimating the superheated electron parameters. However, it remains uncertain whether this underestimation is related to the superthermal electron density or temperature. In the future, we plan to treat superthermal electrons as an input parameter in the fitted model and conduct further adjustments to accurately fit the real superthermal electron parameters.

The comparison of the results demonstrated a remarkable level of consistency with findings from previous result (M. Moncuquet et al. 2020; M. Liu et al. 2023). Specifically, the total electron temperature, fitted with the power-law model $T_e \propto r^{-0.65\pm0.02}$, exhibited a modestly flatter profile compared to the core temperature, which followed $T_c \propto r^{-0.71\pm0.03}$. According to SPANe observations (L. Berčič et al. 2020), there appears to be no significant trend in the variation of strahl electron temperature with radial distance. Additionally, strahl electrons

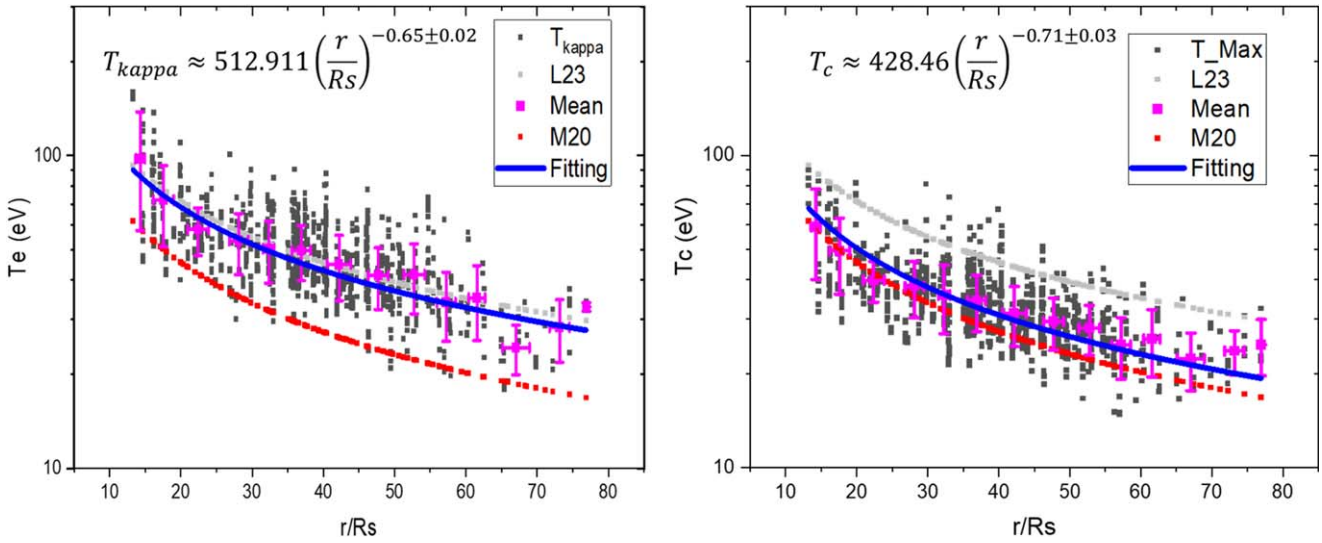

Figure 3. The radial variation of electron temperature within the chosen data set. The left panel illustrates the total electron temperature derived using the kappa function. The right panel displays the core temperature, which is fitted using a two-Maxwellian distribution. The best-fit power laws for these temperatures are as follows: For the total electron temperature, we have $T_e = T_{e0}r^{-0.65\sim-0.67}$; For the core temperature, the power law is $T_c = T_{c0}r^{-0.71\sim-0.74}$.

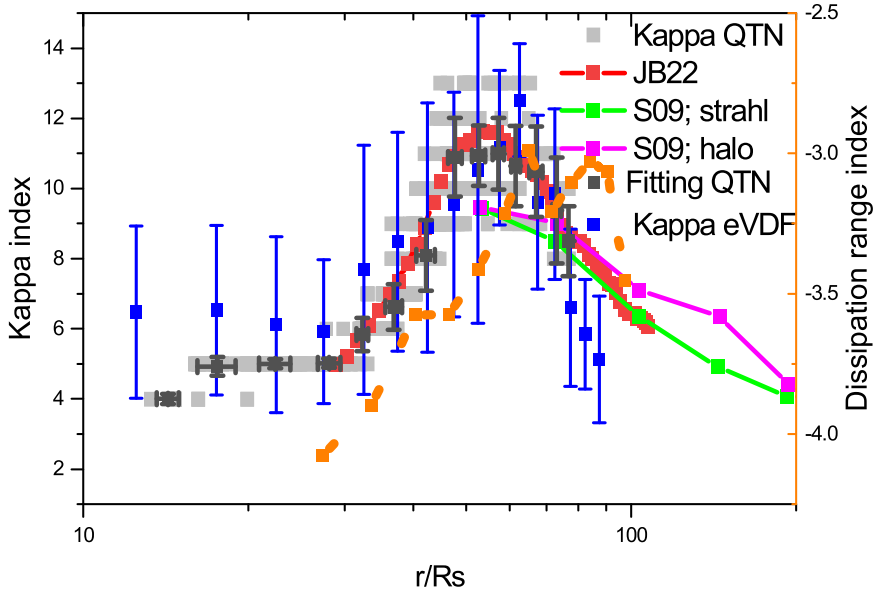

Figure 4. The radial variation of the kappa index in the selected QTN data is shown in gray. The black dots represent the statistical results from each 5 *R*s. The blue line shows the results of direct fitting from SPAN-E data, compared to kappa-fitting results from previous studies represented by the red, green, and pink lines. Note that the orange dashed line represents the turbulent dissipation range index as a function of solar radial distance (S. Lotz et al. 2023). During the fitting process, we constrain the kappa index within the range of [2, 15]. Between 30 *R*s and 60 *R*s, the kappa index experiences an increase, and its trend is essentially consistent with that of the turbulent dissipation range index, indicating a decrease in superthermal electrons within this range. Conversely, beyond 60*R*s, the kappa index decreases, signifying an increase in superthermal electrons within that specific range.

are more prominent as one approaches the Sun, while the density ratio between halo and strahl electrons increases with increasing radial distance (M. Maksimovic et al. 2005; Š. Štverák et al. 2009), implying a scattering of some strahl electrons into halo electrons. Therefore, the flatter T_e profile compared to T_c may primarily result from the flattening of the strahl electron temperature profile. It is worth noting that previous results from the PSP mission (J. B. Abraham et al. 2022) suggest that the physical picture differs somewhat from the simple conversion of strahl to halo electrons seen in Helios observations. PSP findings indicate that the overall suprathermal electron fraction (halo + strahl) increases with heliocentric distance below 0.25 au (where au represents an astronomical unit). Furthermore, the relative densities of halo and strahl electrons are become increasingly small as a function of radial distance near perihelion. However, when in close proximity to the Sun, there are instrumental limitations in measuring both halo and strahl electrons using SPAN-E. Thus, the overall suprathermal fraction (halo+strahl) close to the Sun may be underestimated, and such factors should be handled with greater caution in such scenarios.

4. Superthermal Populations and Energy Flux

4.1. Kappa Index and SPAN-E Data Fitting

In Figure 4, we present the kappa index obtained from our data set as a function of the heliocentric distance. The gray dots represent the results of our QTN fitting; recall that that the kappa index must be a positive integer. As the kappa index

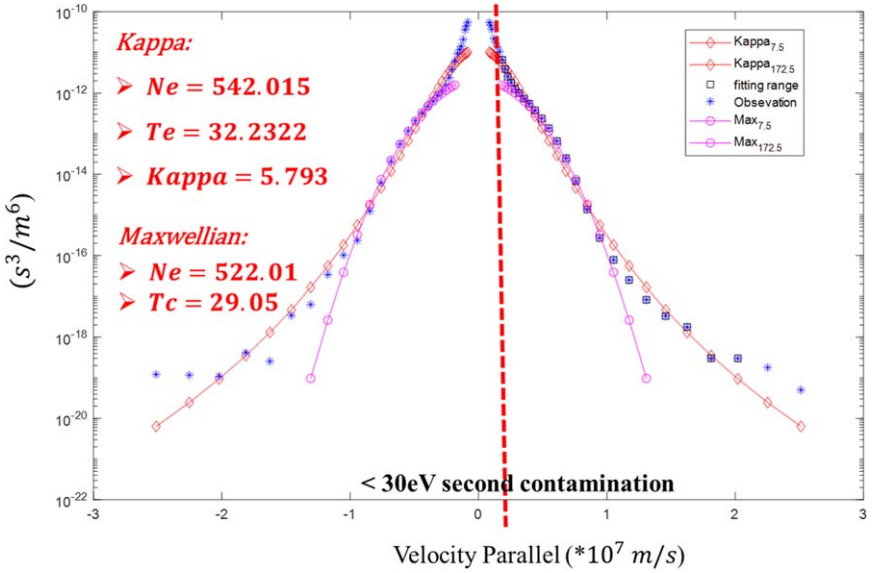

Figure 5. Example of eVDF fitting procedure. The blue dots represent the SPAN-E observational results. The fitting range is indicated by the black square dots, while the red and purple dots depict the results of the kappa and Maxwellian fittings, respectively. That shows in this case the $n_e = 522.02 \pm 0.2$ cm^{-3}, $T_c = 29.05 \pm 0.01$ eV for Maxwellian and for kappa eVDF the $n_e = 542.02 \pm 0.5$ cm^{-3}, $T_e = 32.23\ e \pm 0.01$ V, kappa $= 5.79 \pm 0.1$. It is important to highlight that measurements become unreliable for channels with energies below 30 eV, attributed to secondary contamination of the data by instrument (the 30 eV energy line is delineated by a vertical red line in this graph).

approaches infinity, the distribution becomes more akin to a Maxwellian distribution. The red dots correspond to the fitting results from J. B. Abraham et al. (2022), with the fitting range spanning from 0.13 to 0.5 au. Additionally, the green and pink dots denote the kappa indices for the strahl and halo components, respectively, as reported in the paper by Š. Štverák et al. (2009), which was from Helios I and II. The mean value encompassed by the standard deviation of the kappa index is depicted by the black dots, while the eVDF fitting results are represented by the blue dots. Details of this method are shown in Figure 5, In the context of this study, the kappa index is a critical parameter for accurately modeling the exosphere, especially within the framework of the kinetic exospheric model of the solar wind. The kappa index, which falls within the range of 1.5–15, is particularly significant because it determines the distribution of particle velocities, influencing the behavior of suprathermal particles and the overall dynamics of the solar wind. This is especially important for low kappa values, which are observed in the fast solar wind and directly affect the wind's acceleration to supersonic speeds. The impact of the kappa index has been extensively studied and validated in the literature, including works (H. Lamy et al. 2003; V. Pierrard & J. Lemaire 1996; V. Pierrard et al. 2023), underscoring its importance in both theoretical models and observational data.

Analyzing the results of the kappa index statistical study as depicted in Figure 4, we note a relatively stable variation in the kappa index within the range of 12 to 30 solar radii. However, as we extend the distance to the range of 30 to 60 Rs, the kappa index shows an increase with distance from the Sun, and its trend is essentially consistent with that of the turbulent dissipation range index, the methodology described in the Lotz paper primarily involves calculating and validating both the turbulent inertia region index and the turbulent dissipation region index (identified as the steepest power spectrum index). This is achieved using high-resolution PSP magnetic field power spectrum data, which is then followed by statistical analysis. That means as turbulence intensifies, the eVDF increasingly resembles a Maxwellian distribution due to enhanced particle scattering and energy homogenization mechanisms. This occurs because strong turbulence facilitates the uniform distribution of energy and isotropy in the electron velocity space, thereby driving the eVDFs toward thermal equilibrium. Beyond a distance of 60 solar radii, the kappa index exhibits a continuous decrease. It is noteworthy that beyond 200 solar radii, both κ_strahl ≈ 4 and κ_halo ≈ 2 remain constant (Š. Štverák et al. 2009). This observed relationship between the kappa index and distance suggests a correlation with the solar wind particles velocity distribution function.

For the statistical study and comparing the QTN method results of solar wind properties, we have gathered a large number of measured eVDFs combining observations from SPAN-E data. A detailed description of the full data set and the associated instrument is given in the Appendix. The fitting procedures that we have used for the analysis of the measured eVDFs are use the Global Kappa (M. Maksimovic et al. 1997b; M. Lazar et al. 2017; L. Berčič et al. 2020). Figure 5 is the example of the global kappa-fitting procedures method.

4.2. Solar Wind Energy Flux

The solar wind energy flux (w), which includes the kinetic energy ($w_{\rm kinetic}$), the enthalpy energy ($w_{\rm enthalpy}$) and the flux equivalent to the energy required to overcome the solar gravitation (w_g), and the wave energy flux (w_w), is expressed as:

$$w_{\rm kinetic} = n_p\ m_p\ V_p \frac{V_p^2}{2} + n_a m_a\ V_a\ \frac{V_a^2}{2}, \tag{5}$$

$$w_{\rm enthalpy} = n_e V_p \left(\frac{5k_{\rm B}T_e}{2}\right) + n_p V_p \left(\frac{5k_{\rm B}T_p}{2}\right) + n_a V_a \frac{5k_{\rm B}T_a}{2}, \tag{6}$$

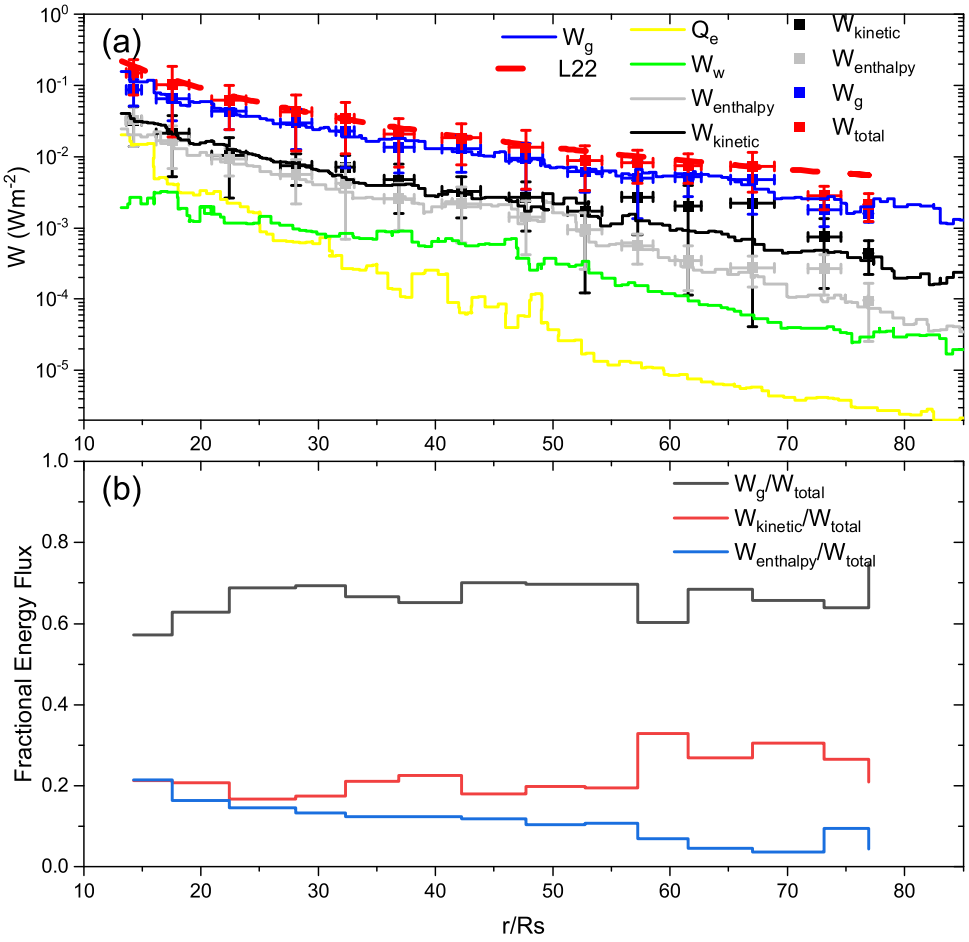

Figure 6. The variation of the solar wind energy flux w and its constituent components with heliocentric distance. The energy values are represented by distinct dots with the squares representing median values surrounded by their standard deviations The red line represents the fitted profile, which aligns with the model and measurement results proposed in the study by M. Liu et al. (2021), $w = (52.1 \pm 1.4)\left(\frac{r}{R_s}\right)^{-1.92\pm0.007}$, (a) is the energy flux as an function of the heliocentric distance, and the dots represent the QTN results and the step line represent the SPAN-E and SPAN-I (wave energy flux) data fitting results, (b) is the fractional energy flux for the w_g, $w_{\rm enthalpy}$, and $w_{\rm kinetic}$.

$$w_g = \left(n_p m_p V_p\left(\frac{GM_s}{R_s}\right) + n_\alpha m_\alpha V_\alpha\left(\frac{GM_s}{R_s}\right)\right)\left(1 - \frac{R_s}{r}\right), \quad (7)$$

$$W_w = \left(\frac{3V_p}{2} + V_A\right) n_p m_p \frac{\langle |z^{\pm}|^2 \rangle}{4}, \quad (8)$$

with the Elsässer variables $z^{\pm} = \delta v \mp \delta b$ (W. M. Elsasser 1950), and the $\pm$ chosen to capture outward-propagating fluctuations (i.e., the minus sign for radially outward magnetic fields, and the plus sign for radially inward magnetic fields). For a more comprehensive analysis of wave energy flux calculations, please refer to the paper by J. S. Halekas et al. (2023). The heat flux (Q) is expressed as:

$$Q_{{\rm heat},e} = \int \frac{1}{2} m v^2 f_e(v) d^3 v. \quad (9)$$

So, the total solar wind energy flux is expressed as:

$$w = w_{\rm kinetic} + w_{\rm enthalpy} + w_g + Q_{{\rm heat},e} + w_w. \quad (10)$$

In the above expression, for all the energy fluxes except for $w_{\rm enthalpy}$, we have neglected the effect of the electron due to its mass being negligible compared to that of the proton. However, for the heat flux, we have only considered the contribution of electrons, as previous reports e.g (J. S. Halekas et al. 2021) indicate that the electron heat flux is significantly larger than the proton heat flux.

Figure 6 displays $w_{\rm total}$, $w_{\rm kinetic}$, $w_{\rm enthalpy}$, and w_g as functions of heliocentric distance in solar radius units (Rs). Our statistical analysis indicates that $w_{\rm total} \approx w_g > w_{\rm kinetic} > w_{\rm enthalpy}$ from the QTN results. However, the total energy flux values decrease as the distance from the Sun increases. Furthermore, we observe that ($w_g \propto r^{-2.0}$) due to the relationship ($n_p\ m_p\ V_p \propto r^{-2.0}$). We excluded the alpha particles from our analysis due to inconsistent availability of radial trends for the alpha populations data. Nonetheless, we calculated the individual partial energies by combining SPAN-E data with a fitting algorithm for the eVDF. The fitting results indicate that the distribution of energy in the energetic components decreases from (w_g) to the heat flux (Q). Statistical results show that the kinetic energy ($w_{\rm kinetic}$) is comparable to the enthalpy ($w_{\rm enthalpy}$) in a small distance range, and both are approximately an order of magnitude greater than the wave energy and 2 orders of magnitude greater than the heat flux energy. In our analysis for the QTN fitting results, we have omitted the consideration of wave energy flux. The total heat flux, denoted as Q, comprises the sum of electron heat flux, q_e, and proton heat flux, q_p. Similar findings were reported in the studies by

M. Liu et al. (2021), J. S. Halekas et al. (2020, 2021), and J. B. Abraham et al. (2022), which indicated that q_e typically falls within the range of 10^{-4} to 10^{-3} Wm^{-2}, while q_p ranges from approximately 10^{-7} to 10^{-5} Wm^{-2} (P. Hellinger et al. 2011). Consequently, these energy flux values are significantly lower compared to other energy flux components. However, in this study, we calculated wave energy and heat flux (Q) utilizing SPAN-E data. The results are presented in Figure 6.

To form a fractional energy flux in Figure 6(b), we utilized the QTN results to calculate the percentage of total energy contributed by each component. In this calculation, we deliberately excluded the heat flux energy (Q) and wave energy flux, focusing solely on the energy required to overcome the solar gravitational potential energy (w_g), kinetic energy ($w_{\rm kinetic}$), and enthalpy energy ($w_{\rm enthalpy}$). From our analysis, the results indicate that (w_g) constitutes approximately 70% of the total energy ($w_{\rm total}$), which is slightly lower than that reported by M. Liu et al. (2021; ∼75% for the heliocentric distance considered). In contrast, the contributions of both $w_{\rm kinetic}$(20%–25%) and $w_{\rm enthalpy}$ (5%–10%) to $w_{\rm total}$ in our analysis are slightly higher compared to previous results (eg., M. Liu et al. 2021). There are two possible reasons accounting for this discrepancy. First of all, the effects of alpha particles are neglected in this work, which may be the main reason causing the underestimation of w_g. Second, the results herein cover a larger time range (from 2018 to 2023) but limited to the periodical unbiased time interval, while M. Liu et al. (2021) makes use of the data sets mainly when the antenna are nominally biased from 2018 to 2020. Both factors may help explain the minor discrepancy, and therefore these results are in rather good agreements considering the uncertainty. Furthermore, these percentages highlight the fundamental roles of gravitational potential energy, kinetic energy, and enthalpy energy in the dynamics and thermodynamic behavior of space plasmas. Gravitational potential energy dominates, making up the majority of the total energy, which is critical for understanding the large-scale behavior and structure of the plasma. Kinetic energy, on the other hand, is essential for describing the motion of particles and the transport of energy within the plasma. Meanwhile, enthalpy energy provides a comprehensive view of the thermodynamic state and energy transitions, offering insights into the thermal energy and heat content of the plasma.

5. Conclusions

In this paper, we explore the variations in the kappa index and solar wind energy flux within the inner heliosphere using observations from PSP. Our analysis encompasses heliocentric distances ranging from 12 Rs to 76 Rs, incorporating data collected during encounters E02 to E13. This comprehensive data set allows us to investigate the behavior of the electron density, temperature, kappa index and solar wind energy flux in the inner heliosphere, providing valuable insights into the mechanisms behind solar wind heating. We have observed that the electron density follows a power law, $n_e \propto (r)^{-2.09}$, and the total temperature exhibits a flattening trend, $T_{\rm kappa} \propto (r)^{-0.65\sim-0.67}$, which contrasts with the core temperature, $T_{\rm core} \propto (r)^{-0.71\sim-0.74}$. Our statistical analysis of the kappa index for solar wind electrons reveals interesting patterns: within the range of 12 to 30 solar radii from the Sun, the kappa index remains relatively constant, approximately kappa $\approx 5 \pm 1$. As we extend to the range of 30 to 60 solar radii, the kappa index increases, this phenomenon aligns with changes in the dissipation range index of turbulence in the region, suggesting that turbulence enhances energy transfer efficiency through improved energy mixing and increased inter-particle interactions (H. Che & M. L. Goldstein 2014; K. Horaites et al. 2019). Consequently, the eVDF moves progressively closer to the thermal equilibrium Maxwell distribution. This process demonstrates how a turbulence-driven system approaches a thermodynamic equilibrium state, and beyond 60 solar radii, it decreases with distance.

Furthermore, our study of solar wind energy flux has shown that $w_g > w_{\rm enthalpy} > w_{\rm kinetic} > Q$, with the Q heat flux contributing about 1.0% to the total energy flux and $w_g \approx 70\% w_{\rm total}$, $w_{\rm kinetic} \approx 20 \sim 25\% w_{\rm total}$, $w_{\rm enthalpy} \approx 5 \sim 10\% w_{\rm total}$. The $w_{\rm kinetic}/w_{\rm total}$ ($w_{\rm enthalpy}/w_{\rm total}$) slightly increases (decreases) with respect to the heliocentric distance, while $w_g/w_{\rm total}$ is almost conserved for the heliocentric distance considered. This is in agreement with the fact that the pristine solar wind detected by PSP is still under acceleration and gets cooler during the expansion. These findings align with previous results obtained from long-term observations at greater distances and various latitudes (R. Schwenn & E. Marsch 1990; G. Le Chat et al. 2009, 2012; D. J. McComas et al. 2014). Specifically, both the actual percentages of different energy flux types and their radial trend are in rather good agreements with the recent results reported by M. Liu et al. (2021), considering the different ways to deal with alpha particle effects and the slightly different time intervals used for analysis. We await more data that are to come in the future PSP encounters, with the recovery of the well calibrated alpha parameters. And it is widely employed in global hemispheric studies and modeling to deduce density from solar wind speed (and vice versa), as supported by various studies (D. J. McComas et al. 2017, 2020; F. Shen et al. 2018; S. M. Krimigis et al. 2019; Y. Wang et al. 2020).

In the future, we plan to employ exospheric models alongside the measured kappa index to compute variations in plasma parameters and solar wind along the radial of the Sun. That will be enhancing the consideration of solar wind acceleration. Furthermore, our research team aims to broaden the study's scope by investigating solar wind velocity statistics at various latitudes, thereby advancing our comprehension of solar wind dynamics.

Acknowledgments

This work was supported by the National Key R&D Program of China under grant 22022YFE03070004, Strategic Priority Research Program of Chinese Academy of Sciences (grant XDB 41000000), the National Natural Science Foundation of China (NSFC) grants 41974168 and 42174203, the Guangdong Pearl River Talent Program (2019QN01G838), Pioneer project of China National Nuclear Power Corporation, and Shenzhen Science and Technology Program (grant JCYJ20210324104810027). V.P. acknowledges the project 21GRD02 BIOSPHERE from the European Partnership on Metrology, co-financed by the European Union's Horizon Europe Research and Innovation Programmer and by the participating states. We also thank the PSP mission for the use of FIELDS and SPAN data in this study.

Appendix
Comparative Analysis of Measurement Results Using QTN Fit and eVDF Fit

To facilitate the comparison of measurement results, we employed both QTN fit and eVDF fit methodologies (G. Le Chat et al. 2009; M. Lazar et al. 2017; J. B. Abraham et al. 2022). It is important to note that the quantity of data and the duration of the measurements were not identical for both approaches. Table A1 presents the respective data sets for QTN fit and eVDF fit, allowing for a comprehensive examination of the obtained results.

In this data set, accurately calculating the actual kappa index value is not feasible when the FIELDS is biased due to computational constraints. The kappa value is generally influenced by the relative magnitudes of the peaks in the power spectrum. Specifically, when a current bias is applied, the power spectrum signal at low frequencies becomes elevated, contaminating the true peak signal. Consequently, this approach is not suitable for accurately determining the actual kappa index when current bias is present. Further details regarding the variation of QTN under bias conditions will be presented in our future work.

Table A1
The Kappa Values Calculated in this Study are Presented Below, Obtained Using Two Different Methods: QTN and eVDF

Method	Instrument	Biased/Unbiased	Period	Samples
QTN	FIELDS	Unbiased	E2 ∼ E13	≈1300
eVDF	SPAN-E	⋯	E1 ∼ E13	≈400,000

Note. The following table provides the statistical status of the instruments used in these methods and their corresponding statistical quantities.

ORCID iDs

Xianming Zheng https://orcid.org/0009-0005-7089-9749
Viviane Pierrard https://orcid.org/0000-0001-5014-7682
Kristopher G. Klein https://orcid.org/0000-0001-6038-1923
Mingzhe Liu https://orcid.org/0000-0003-2981-0544
Joel B. Abraham https://orcid.org/0000-0002-6305-3252

References

Abraham, J. B., Owen, C. J., Verscharen, D., et al. 2022, ApJ, 931, 118
Bale, S. D., Badman, S. T., Bonnell, J. W., et al. 2019, Natur, 576, 237
Bale, S. D., Goetz, K., Harvey, P. R., et al. 2016, SSRv, 204, 49
Berčič, L., Larson, D., Whittlesey, P., et al. 2020, ApJ, 892, 88
Chateau, Y. F., & Meyer-Vernet, N. 1991, JGR, 96, 5825
Che, H., & Goldstein, M. L. 2014, ApJL, 795, L38
Elsasser, W. M. 1950, RvMP, 22, 1
Fejer, J. A., & Kan, J. R. 1969, RaSc, 4, 721
Gurnett, D. A. 1998, in Measurement Techniques in Space Plasmas: Fields. Geophysical Monograph, ed. R. F. Pfaff, J. E. Borovsky, & D. T. Young, Vol. 103 (Washington, DC: AGU), 121
Halekas, J. S., Bale, S. D., Berthomier, M., et al. 2023, ApJ, 952, 26
Halekas, J. S., Whittlesey, P. L., Larson, D. E., et al. 2021, A&A, 650, A15
Halekas, J. S., Whittlesey, P., Larson, D. E., et al. 2020, ApJS, 246, 22
Hellinger, P., Matteini, L., Štverák, Š., Trávníček, P. M., & Marsch, E. 2011, JGRA, 116, A09105
Hoang, S., Steinberg, J. L., Epstein, G., et al. 1980, JGR, 85, 3419
Horaites, K., Boldyrev, S., & Medvedev, M. V. 2019, MNRAS, 484, 2474
Issautier, K., Le Chat, G., Meyer-Vernet, N., et al. 2008, GeoRL, 35, L19101
Issautier, K., Meyer-Vernet, N., Moncuquet, M., & Hoang, S. 1998, JGR, 103, 1969
Issautier, K., Meyer-Vernet, N., Moncuquet, M., Hoang, S., & McComas, D. J. 1999, JGR, 104, 6691
Issautier, K., Moncuquet, M., & Hoang, S. 2004, SoPh, 221, 351
Issautier, K., Moncuquet, M., Meyer-Vernet, N., Hoang, S., & Manning, R. 2001, Ap&SS, 277, 309
Issautier, K., Perche, C., Hoang, S., et al. 2005, AdSpR, 35, 2141
Kellogg, P. J. 1981, PlPh, 23, 735
Krimigis, S. M., Decker, R. B., Roelof, E. C., et al. 2019, NatAs, 3, 997
Lazar, M., Pierrard, V., Shaaban, S., Fichtner, H., & Poedts, S. 2017, A&A, 602, A44
Lamy, H., Pierrard, V., & Maksimovic, M. 2003, JGR, 108, 1047
Le Chat, G., Issautier, K., & Meyer-Vernet, N. 2012, SoPh, 279, 197
Le Chat, G., Issautier, K., Meyer-Vernet, N., & Hoang, S. 2011, SoPh, 271, 141
Le Chat, G., Issautier, K., Meyer-Vernet, N., et al. 2009, PhPl, 16, 102903
Le Chat, G., Issautier, K., Meyer-Vernet, N., et al. 2010, in AIP Conf. Proc. 1216, 12th Int. Solar Wind Conf. (Melville, NY: AIP), 316
Liu, M. 2022, PhD thesis, Université Paris Sciences et Lettres
Liu, M., Issautier, K., Meyer-Vernet, N., et al. 2021, A&A, 650, A14
Liu, M., Issautier, K., Moncuquet, M., et al. 2023, A&A, 674, A49
Livi, R., Larson, D. E., Kasper, J. C., et al. 2022, ApJ, 938, 138
Lotz, S., Nel, A. E., Wicks, R. T., et al. 2023, ApJ, 942, 93
Maksimovic, M., Bale, S. D., Bercic, L., et al. 2020, ApJS, 246, 62
Maksimovic, M., Gary, S. P., & Skoug, R. M. 2000, JGR, 105, 18337
Maksimovic, M., Hoang, S., Meyer-Vernet, N., et al. 1995, JGR, 100, 19881
Maksimovic, M., Pierrard, V., & Lemaire, J. F. 1997a, A&A, 324, 725
Maksimovic, M., Pierrard, V., & Riley, P. 1997b, GeoRL, 24, 1151
Maksimovic, M., Zouganelis, I., Chaufray, J.-Y., et al. 2005, JGRA, 110, A09104
Marsch, E. 2006, LRSP, 3, 1
Marsch, E., Pilipp, W., Thieme, K., & Rosenbauer, H. 1989, JGRA, 94, 6893
Martinović, M. 2016, PhD thesis, Univ. Belgrade
Martinović, M. M., Dordevic, A. R., Klein, K.G., et al. 2022, JGRA, 127, e30182
Martinović, M. M., Klein, K. G., Gramze, S. R., et al. 2020, JGRA, 125, e28113
Martinović, M. M., Zaslavsky, A., Maksimovic, M., et al. 2016, JGRA, 121, 129
McComas, D. J., Allegrini, F., Bzowski, M., et al. 2014, ApJS, 213, 20
McComas, D. J., Bzowski, M., Dayeh, M. A., et al. 2020, ApJS, 248, 26
McComas, D. J., Zirnstein, E. J., Bzowski, M., et al. 2017, ApJS, 229, 41
Meyer-Vernet, N. 1979, JGR, 84, 5373
Meyer-Vernet, N., Issautier, K., & Moncuquet, M. 2017, JGRA, 122, 7925
Meyer-Vernet, N., & Perche, C. 1989, JGR, 94, 2405
Moncuquet, M., Lecacheux, A., Meyer-Vernet, N., Cecconi, B., & Kurth, W. S. 2005, GeoRL, 32, L20S02
Moncuquet, M., Matsumoto, H., Bougeret, J.-L., et al. 2006, AdSpR, 38, 680
Moncuquet, M., Meyer-Vernet, N., Issautier, K., et al. 2020, ApJS, 246, 44
Novaco, J. C., & Brown, L. W. 1978, ApJ, 221, 114
Parker, E. N. 1958, ApJ, 128, 664
Phillips, J. L., Bame, S., Gary, S., et al. 1995, in Proc. 28th ESLAB Symp., The High Latitude Heliosphere (Dordrecht: Kluwer), 109
Pierrard, V., & Lazar, M. 2010, SoPh, 267, 153
Pierrard, V., & Lemaire, J. 1996, JGR, 101, 7923
Pierrard, V., Péters de Bonhome, M., Halekas, J., et al. 2023, Plasma, 6, 518
Pilipp, W. G., Miggenrieder, H., Mühläuser, K. H., Rosenbauer, H., & Schwenn, R. 1990, JGRA, 95, 6305
Pulupa, M., Bale, S. D., Bonnell, J. W., et al. 2017, JGRA, 122, 2836
Salem, C., Bosqued, J. M., Larson, D. E., et al. 2001, JGR, 106, 21701
Schwenn, R., & Marsch, E. 1990, Physics of the Inner Heliosphere I: Large Scale Phenomena (Berlin: Springer), 99
Shen, F., Yang, Z., Zhang, J., Wei, W., & Feng, X. 2018, ApJ, 866, 18
Štverák, Š., Maksimovic, M., Trávníček, P. M., et al. 2009, JGRA, 114, A05104
Verscharen, D., Klein, K. G., & Maruca, B. A. 2019, LRSP, 16, 5
Wang, Y., Guo, X., Wang, C., et al. 2020, SpWea, 18, e02262
Whittlesey, P. L., Larson, D. E., Kasper, J. C., et al. 2020, ApJS, 246, 74
Woodham, L., Horbury, T. S., Matteini, L., et al. 2021, A&A, 650, L1
Zaslavsky, A., Meyer-Vernet, N., Hoang, S., Maksimovic, M., & Bale, S. D. 2011, RaSc, 46, RS2008
Zheng, X., Liu, K., Martinovic, M. M., et al. 2024, ApJ, 963, 154
Zouganelis, I., Maksimovic, M., Meyer-Vernet, N., Lamy, H., & Issautier, K. 2004, ApJ, 606, 542
Zouganelis, I., Maksimovic, M., Meyer-Vernet, N., et al. 2010, RaSc, 45, RS1005